

# Extended Emission Line Gas in Radio Galaxies - PKS0349-27

B. I. Grimberg

*Michigan State University, East Lansing MI 48824-1116*

E. M. Sadler <sup>1</sup>

*School of Physics, University of Sydney, NSW 2006, Australia*

and

S. M. Simkin <sup>1</sup>

*Michigan State University, East Lansing, MI 48824-1116*

## ABSTRACT

PKS0349-27 is a classical FRII radio galaxy with an AGN host which has a spectacular, spiral-like structure in its extended emission line gas (EELG<sup>2</sup>). We have measured the velocity field in this gas and find that it splits into 2 cloud groups separated by radial velocities which at some points approach 400 km s.<sup>-1</sup> Measurements of the diagnostic emission line ratios [OIII] 5007/H $\beta$ , [SII] 6716+6731/H $\alpha$ , and [NII] 6583/H $\alpha$  in these clouds show no evidence for the type of HII region emission associated with starburst activity in either velocity system. The measured emission line ratios are similar to those found in the nuclei of narrow-line radio galaxies, but the extended ionization/excitation cannot be produced by continuum emission from the active nucleus alone. We present arguments which suggest that the velocity disturbances seen in the EELG are most likely the result of a galaxy-galaxy collision or merger but cannot completely rule out the possibility that the gas has been disrupted by the passage of a radio jet.

*Subject headings:* galaxies: active — galaxies: interactions — galaxies: individual (PKS0349-27) — galaxies: ISM — galaxies: kinematics and dynamics — radio lines: galaxies

---

<sup>1</sup>Visiting Astronomer, Cerro Tololo Inter-American Observatory. CTIO is operated by AURA, Inc. under contract to the National Science Foundation.

<sup>2</sup>We have chosen this designation rather than the more common abbreviation EELR(egions) because we wish to emphasize the physical difference between this type of highly extended gas and the extended narrow line regions around the nuclei of active galaxies.

## 1. Introduction

PKS0349-27 is a prime example of a classical, double-lobed (FR II) radio galaxy (Bolton et al. 1965, Christiansen et al. 1977) with a narrow emission line nuclear spectrum. It is also a spectacular example of a radio AGN host with an extended gaseous component which has a structure reminiscent of a barred spiral (Hansen et al. 1987, Baum et al. 1988, Simkin and Sadler 1989; see Figure 1b in section 2.1). It has a redshift of  $\sim 19800 \text{ km s}^{-1}$  (Searle and Bolton 1965), corresponding to a scale of  $\sim 0.96 \text{ kpc } (")^{-1} h^{-1}$ . This galaxy appears to fit into the “rotator” class of FR II, double-lobed, radio galaxies defined by Baum et al. 1988.

### 1.1. Previous Observations

Earlier kinematic studies of this object have suggested that its centrally concentrated ionized gas is in rapid rotation as well as expansion (with a rotation axis at  $\sim \text{PA}140\text{-}180^\circ$ , Danziger et al. 1984, Tadhunter et al. 1989). Its non-nuclear spectrum has been extensively observed (op cit. and Robinson et al. 1987, Storchi-Bergmann et al. 1996, Binette et al. 1996) and incorporated in several analytical discussions of the type of ionization/excitation conditions found in the non-nuclear regions of active galaxies (op cit. and Viegas and de Gouveia Dal Pino 1992, Wilson et al. 1997). On the basis of HST, UV continuum images, Zirbel and Baum 1998 have concluded that there is no strong UV emission from its nucleus; however, they do report some evidence for extended UV emission in the  $\sim 3''$  region surrounding the nucleus.

Detailed radio continuum images of this object have been published by Ekers et al. 1989 at 4.89 GHz and by Baum et al. 1988 at 1400 MHz.

### 1.2. EELG, Mergers, and Star Formation

Although it was initially thought to be a rare phenomenon, the presence of EELG is quite common in many strong radio galaxy hosts (as reviewed and discussed by Baum and Heckman 1989a). It may well be related to the “alignment” effect seen in more distant, powerful radio galaxies (cf. McCarthy et al. 1995, McCarthy et al. 1996, Best et al. 1996) and frequently seems to reflect a different kinematic system from the stellar component of the radio galaxy host (cf. the reviews in Baum and Heckman 1989a, and Tadhunter et al. 1989).

Ideas about the origins of this gas, its ionization/excitation parameters, and kinematic properties are reviewed in the references cited above as well as Koekemoer and Bicknell 1998, and Tadhunter et al. 1998. These can be briefly summarized as follows:

1. Origins: The gas may be native, from stellar mass loss; acquired in a “cooling flow;” accreted from primordial cold gas; or acquired from a gas-rich galaxy in a merger or close encounter.
2. Ionization/excitation: The gas may be photoionized by a hard continuum source originating in the nucleus; shock heated by collisional impact due to radio jets or tidal disturbances from a merger or close encounter and post shock, radiative re-heating; photoionized by starburst activity; or a combination of these.
3. Kinematics: The gas may be in stable orbits about the host; disrupted by collisions arising from mergers and tidal disruption; or disrupted by the impact of a radio jet.

Nearby objects are particularly important for resolving the complex interactions noted above because high spatial resolution is needed to distinguish between the different physical zones which can arise within the clouds. The number of nearby, intrinsically powerful radio sources is, however, limited and thus it is important to subject those which do exist to intense analysis. This implies that these nearby objects should be restudied as instrumental capabilities improve our ability to measure such objects more accurately and with higher resolution.

### 1.3. Overview of the Present Study

PKS0349-27 is one of the few objects which is close enough for such detailed study and which also displays an extensive, highly structured ionized gas region in its host galaxy. In this paper we report new imaging and spectroscopic data for this object which identify regions of extreme kinematic disruption in the EELG of this galaxy’s host. The analysis of these data is described in sections 2.1 and 2.2. The implications of the observed kinematics and diagnostic emission line ratios for the origin and ionization/excitation of this galaxy’s EELG are discussed in sections 3.2, 3.3, and 3.4.

## 2. Observations and Data Analysis

As part of a program to examine the complex kinematics in FR II radio galaxies we obtained narrow band  $H\alpha$  and continuum images and long slit spectra of PKS0349-27 with the CTIO 1.5m and 4m telescopes. The record of these observations is summarized in Table 1.

### 2.1. Optical Images

Direct images of PKS0349-27 were taken in January 1988 with the CTIO 1.5m,  $888 \times 800$  TI CCD (binned to  $444 \times 400$ ) and  $f/13.5$  cassegrain secondary (lines 1 to 4 in Table 1). The CCD scale was  $0.31'' px^{-1}$ . The galaxy was observed through matched on-band off-band filters with the aim of minimizing PSF differences between the image sets. The paired images were reduced using the routines in the IRAF ccdred package and STSDAS wfpc, crrej, which did an excellent job of removing “cosmic rays.” The resulting, composite continuum image is shown as a logarithmic grayscale plot in Figure 1a. The continuum image was fit with the STSDAS isophote routine to produce a model continuum galaxy, which was then subtracted from the  $H\alpha$  image, yielding the model-subtracted image shown (as grayscale) in Figure 1b. This technique leaves intact the continuum sources, such as stars and other galaxies, which are not directly associated with the extended continuum of the host galaxy, but improves visibility of faint emission features by minimizing subtraction-induced noise.

A clearer picture of the relationship between the optical  $H\alpha$  image and the radio structure is shown in Figure 2. Figure 2a is a 20 cm VLA radio continuum image (Simkin and Calcutt 1995), and Figure 2b is the continuum subtracted (not model subtracted)  $H\alpha$  image. We note that all of the other “sources” in the field subtract out in Figure 2b, indicating that they are either pure continuum sources or emission line sources at a redshift which differs from that of PKS0349-27 by at least  $1700 \text{ km s}^{-1}$ . Figure 2c is a superposition of the  $H\alpha$  image on the 20 cm image with the galaxy nucleus marked as a cross. The host galaxy is clearly displaced towards the brighter (NE) radio lobe, which has a hot spot that is seen in the 4.89 GHz map published by Ekers et al. 1989. The faint arcs (marked as  $f1$ ,  $f2$ , and  $f3$  in Figure 2b) are also present in the [OIII] image of Hansen et al. 1987. The feature designated  $f2$  corresponds to the region designated “C” by Robinson et al. 1987. We note

that the features  $f1$  and  $f2$  appear to be parallel to the polarization vectors seen in the 20 cm VLA map of Baum et al. 1988. Although this alignment may not be significant, it does suggest the possibility that the extended radio plasma may be interacting with the ionized gas in this region.

### 2.2. Optical Spectroscopy

Three long-slit spectra were taken during two consecutive nights in February 1987 with the CTIO 4m spectrograph and the TI CCD. All exposures were bracketed with spectra of a HeArNe arc lamp taken with the spectrograph in the same PA as the galaxy spectrum and the telescope at the sky positions corresponding to the start and end positions for the intervening galaxy spectrum. The slit positions and observing details are shown in lines 5 through 7 in Table 1. In all cases, the scale along the slit was  $0.73'' px^{-1}$  and the slit width was  $180 \mu\text{m}$  ( $1.2''$ ). Slit positions, widths and coverage are shown superimposed on the continuum image in Figure 1a. Calibration stars (LTT1788 and LTT3864) were taken at the beginning and end of each night.

The slit in PA  $83^\circ$  covers the extended arm-like features seen in the host (shown in Figure 1b) but does not lie along the radio axis, which is, instead, aligned along the inner bar-like structure near the nucleus. The direction of the radio axis is indicated by the dark bar in PA  $56^\circ$  in Figure 1a. At radial distances which lie between 7 and 14 kpc  $h^{-1}$  from the nucleus, the spectra for PA  $83^\circ$  exhibit strong bifurcation in the spatially extended emission lines. An image of the stronger spectral features for the extended emission line regions in this PA is shown in Figure 3. The extreme distortions show up in both the permitted lines of  $H\alpha$  (Figure 3b) and the forbidden lines of [OIII] and [NII] (Figure 3a and b). Knots labeled A and B in Figure 2b correspond to the bifurcated spectral lines in Figure 3, which are marked A1 and B2. These are found at velocities which are close to the nuclear velocity and hereafter will be designated “lo-vel” clouds. The regions in the spectral lines marked A2 and B1 are found at velocities with much higher amplitudes relative to the nucleus, and hereafter will be designated “hi-vel” clouds. Since these velocity anomalies appear in both the “red” spectra as well as the “green” spectra which were taken on different nights, they are certainly real.

### 2.2.1. Velocities

The spectra were reduced using a set of interactive routines (written by SMS). They were flat fielded, calibrated in wavelength, calibrated for S-distortion, which was minimal, and rebinned to remove S-distortion and to produce constant wavelength increments. A sinc function was used for this rebinning. This is the proper interpolation function for this type of evenly sampled spectral data, since it mimics the slit function and has a modulation transfer function tailored to finite data arrays. The wavelength ranges and dispersions are given in lines 5-7 of Table 1.

The internal consistency in the fits to the calibration spectra was roughly 0.25 pixels, corresponding to  $\pm 0.37 \text{ \AA}$  for the  $\lambda\lambda 4895\text{-}5745$  spectrum and  $\pm 0.30 \text{ \AA}$  for the  $\lambda\lambda 6653\text{-}7338$  spectra. These translate into velocity errors of  $\sim 21 \text{ km s}^{-1}$  and  $\sim 14 \text{ km s}^{-1}$  respectively. Emission line positions in the calibrated spectra were measured using an interactive routine which was adapted from analysis routines developed by K. Ford at Carnegie Institution of Washington. This routine finds the line peak, calculates the line centroid and the center of a gaussian fit to its profile after background subtraction, and automatically steps onto the next radial distance along the direction perpendicular to the slit until the selection criteria are no longer met. The routine allows interactive setting of selection criteria and baseline intervals. The velocities reported here are based on measurements which have line strengths in excess of 10 times the rms in the baseline background and which agree to within 0.5 pixels between emission line positions determined by the two positioning routines. While analyzing the data, it became clear that the emission lines closer to the nucleus were composed of multiple peaks, representing at least 2 separate velocity systems. These peaks were measured using line plots and an interactive cursor and are discussed in the next paragraph. The error for these latter measurements cannot be determined but is clearly greater than that for wavelength calibration fits and probably greater than that for line fitting further out from the nucleus.

The systemic velocity from these measurements, obtained from the strongest emission lines – [SII], [NII],  $\text{H}\alpha$ , and [OIII] – is  $19846 \pm 72 \text{ km s}^{-1}$ . This is in surprisingly good agreement with the value of  $19846 \pm 130 \text{ km s}^{-1}$  found by Storchi-Bergmann et al. 1996 with lower resolution spectra. The error of

$\pm 72 \text{ km s}^{-1}$  however, far exceeds the value of  $\sim 14$  to  $21 \text{ km s}^{-1}$  for the calibration spectra and that of  $\pm 21 \text{ km s}^{-1}$  observed for other emission line galaxies measured with the same equipment over two different seasons (cf. Simkin et al. 1999a). Inspection of the nuclear spectra shows that there are, in fact, at least two separate velocity systems; at  $19840 \pm 14 \text{ km s}^{-1}$  and  $19908 \pm 18 \text{ km s}^{-1}$ ) and possibly a third, at  $19708 \text{ km s}^{-1}$  seen only in the [SII] lines. Thus, the velocity measurements reported here have been zeroed to a nuclear redshift velocity of  $19800 \text{ km s}^{-1}$  for purposes of determining the internal kinematics.

The measured velocities are plotted in Figure 4. The error bars have been omitted in this plot to allow cleaner delineation of the different line species. The scatter in the nuclear velocity measurements noted above is clearly seen in Figure 4a and appears to be associated with the velocity bifurcations seen at larger radii. The separate velocity systems are also seen in the PA  $146^\circ$  spectrum but are easily lost in the steep velocity gradient across the nucleus in that position angle (Figure 4b). This suggests that the dispersion in cloud velocities seen in the nuclear spectrum in both position angles is more likely the result of limited spatial resolution than true radial superposition of differentially moving clouds. The bifurcated velocities for the clouds labeled A1, A2, B1, and B2 in Figure 3a are marked in Figure 4a.

### 2.2.2. Emission Line Ratios

PA  $83^\circ$  was the only position angle which was observed in *both* the red and the blue-green spectral region. The line ratios from these spectra for the emission lines [OIII] 5007/ $\text{H}\beta$ , [SII] 6716+6731/ $\text{H}\alpha$ , and [NII] 6583/ $\text{H}\alpha$  are shown in Table 2. In most cases only lines with signal to noise (S/N)  $\geq 3$  were measured. In a few cases this criterion was relaxed to  $\text{S/N} \simeq 2$ . All errors listed in Table 2 reflect  $1\sigma$  fluctuations from the measured line strengths. We note, however, that an occasional single emission line measurement can have an erroneous value which is well outside this error limit if it has been contaminated by a weak “cosmic ray” hit. The [OI] 6300 emission line is seen not only in the nuclear spectrum of this object, but is also visible as an extended feature, with the same characteristic shape as the stronger emission lines shown in Figure 3. Although detectable as a continuous feature in video images of the spectrum (and recorded by Robinson et al. 1987), this line is far too weak in our observed ccd spectrum to meet

the criteria imposed on the measurements reported in Table 2.

Although we observed flux calibration standards for all of these spectra, it is clear from examination and comparison of these calibration spectra from night to night that the nights were non-photometric, with flux variations of a factor of 2 or 3 from one night to the next and up to 1.5 on the same night. Thus it is not possible to obtain meaningful absolute values for the emission line strengths nor is it possible to obtain meaningful flux ratios for emission lines, such as  $[\text{OI}]\lambda 6300$  and  $[\text{OIII}]\lambda 5007$ , which were taken with different grating settings on different nights. We have, however, determined the *relative* corrections to the ratios in Table 2 using the published absolute flux values for the stars observed. Even in the most extreme case of  $[\text{OI}]/\text{H}\alpha$  these are less than  $\pm 0.04$  in the log. Since this is much less than the errors from “noise” for most of the observed emission lines, any error in the *relative* calibration will be dominated by the emission line measurement errors themselves. We reiterate here the important observational point made by Veilleux and Osterbrock 1987: Absolute flux measurements are very difficult to accomplish, while diagnostic line ratios for adjacent emission lines observed simultaneously can be very accurate.

The measured line ratios in Table 2 are plotted in a series of “BPT” diagrams (cf. Baldwin et al. 1981, and Veilleux and Osterbrock 1987), shown in Figures 5, 4, and 4. These plots will be described and discussed in detail in section 3.3. In addition to the logarithmic line ratios in Table 2, we have calculated the line ratios for the  $[\text{SII}]\lambda\lambda 6716/6731$  doublet which can be used to estimate the gas cloud densities. Although the errors are substantial for any one value of this ratio, the general *trends* in this density indicator are significant. If the EELG is optically thin and has a constant temperature, a trend toward higher values of the line ratio implies a trend towards lower values in the gas density (cf. Osterbrock 1989). However, Ferguson et al. 1997 have found that for clouds with stratified densities and temperatures this line ratio may not be useful as a density indicator. The  $[\text{SII}]$  line ratios are plotted, with low and high density limits marked, in Figure 6a and they are discussed in section 3.3.2 below.

### 3. Discussion

As noted in section 1.2 there are several different scenarios involving the formation and fueling of radio galaxies which may be relevant to an interpretation of the EELG in this object. In broad outline they are:

1. Possible galaxy collisions, mergers, and tidal forcing of the extended gas by a nearby companion.
2. Ionization and excitation of the EELG by continuum radiation from the nuclear “engine”.
3. Interaction between a radio plasma jet and the interstellar medium in the host galaxy.

All of these possibilities have been discussed for PKS0349-27 in earlier papers (cf. Danziger et al. 1984, Robinson et al. 1987, Tadhunter et al. 1989, Viegas and de Gouveia Dal Pino 1992, Storchi-Bergmann et al. 1996 and Wilson et al. 1997). However, the present data, with their better spectral resolution, provide additional information with new implications for these various scenarios.

#### 3.1. Morphological Structure of the Ionized Gas - Tides?

There are several studies in the literature which support the idea that AGNs are fueled by infalling material which has been channeled into a galaxy’s nuclear regions by a merger or other tidal disturbance (cf. MacKenty et al. 1994 and references therein). However, the short time scales involved in this process and the fact that some mergers and tidal disturbances *do not* fuel AGNs make it difficult to assess the importance of this mechanism for radio galaxies. There are several known examples of candidates for galaxy mergers in non-radio galaxies which show that the extended ionized gas in these systems is photoionized by starburst activity (Carilli et al. 1989, Carilli et al. 1994, Hibbard et al. 1994, Hibbard and Van Gorkom 1996, Arnaboldi et al. 1997). Thus, starbursts may be one way of identifying merger activity in AGN hosts.

The long, two-armed structure of the ionized gas, shown in Figures 1b and 4b, and the  $[\text{OIII}]$  images of Hansen et al. 1987 and Baum et al. 1988, is similar to the type of structure associated with tidally interacting galaxies (Toomre 1977, Byrd and Klarić 1990 and references therein). The suggestion of tidal

interaction is reinforced by the presence of a companion galaxy with a radial velocity within  $\sim 200 \text{ km s}^{-1}$  of the PKS0349-27 host which is seen at the end of the object’s eastern arm in Figure 1b. This was first identified by Danziger et al. 1984, who measured its redshift. If the structure of the EELG is determined by a tidal encounter or a merger, then the most likely geometry is one in which we are viewing the orbit of the merging companion nearly edge-on (cf. Toomre 1977, Byrd and Klarić 1990). Such systems often have gas velocities which are bifurcated or counter rotational (op cit.).

### 3.2. Ionized Gas Velocities

The data plotted in Figure 4a show that the most notable split in velocities occurs for gas at  $R > 7 \text{ kpc } h^{-1}$ . This type of velocity detail was not identified in earlier measurements of this object (Danziger et al. 1984, Tadhunter et al. 1989, Storchi-Bergmann et al. 1996), either because it is peculiar to this particular position angle, unresolved in the earlier spectra, or because the line intensities in the low velocity system are weaker than in the high velocity one. Since the extreme velocity separation of  $\sim 1000 \text{ km s}^{-1}$  between the systems in A1 and B2 is far in excess of any velocity amplitudes reported by either Danziger et al. 1984 or Tadhunter et al. 1989 for the gas at PA  $90/270^\circ$  it appears likely that these earlier data refer to gas clouds associated with those labeled A2 and B1 in Figures 3 and 4. Because these two systems (A2 and B1) are also stronger (Figure 3), the presence of the weaker systems (A1 and B2) in other position angles cannot be ruled out by these earlier measurements. Finally, although the split in velocity systems is most notable for the knots labeled A and B in Figure 2b, the velocity points in Figure 4a as well as the discussion in section 2.2.1 show that this separation in cloud velocities extends into regions closer to the nucleus, but with much smaller amplitude. Thus, there is a strong possibility that *both* velocity systems are present throughout the host galaxy but the weaker one has been undetected until now.

Danziger et al. 1984 present a composite rotation-expansion model for the gas in the host of PKS349-27. Although the “rotation” velocities in Figure 4b (PA  $146^\circ$ ) are roughly consistent with that earlier model, the bifurcated velocities shown in Figure 4a (PA  $83^\circ$ ) show that the situation is much more complex than simple rotation-expansion. As a first step in resolving this complexity, we believe it is important to try to

determine which of the different velocity clouds are physically associated. The two most likely patterns for the gas velocities shown in Figure 4a are: (1) The clouds comprising sets A2 and B2 may be physically associated with a high redshift (“hi-z”) system with respect to the host nucleus; while those in A1 and B1 comprise a low redshift (“lo-z”) system. (2) The extreme velocity clouds for the set A1 and B2 may be physically associated with a system which has a high rotational velocity relative to the host galaxy nucleus (“hi-vel” clouds), while the clouds (A2 and B1), comprise a separate, independent system with relatively low rotational velocities (“lo-vel” clouds).

### 3.3. Line Ratios - Ionization and Excitation

We have used the BPT plots of measured emission line ratios in Figures 5, 4, and 4 to try to delineate the relationship between the different cloud systems. The solid curves in each diagram in Figures 5 through 4 are taken from Veilleux and Osterbrock 1987, and mark the empirical division between HII-region like objects, which lie to the left hand side of the line, and objects, such as AGNs, ionized by a harder radiation spectrum, which lie to the right hand side of the line.

#### 3.3.1. Star Formation?

First, in an attempt to identify any gross differences in the physical conditions between the EELG, we have separated the emission line measurements into two different sets according to radial distance from the nucleus. Those with projected distances  $> 7 \text{ kpc } h^{-1}$  from the nucleus (Figures 5a and b) are plotted with the “hi-vel” clouds (A1 and B2) as filled symbols and the “lo-vel” clouds as open symbols. Those with projected distances  $< 7 \text{ kpc } h^{-1}$  from the nucleus (Figures 5c and d), are plotted with points to the west of the nucleus marked as filled symbols and points to the east of the nucleus marked as open symbols.

Figure 5 allows us to immediately test the hypothesis that one of the velocity systems arises from gas which has been disturbed (either by the radio plasma or as infall from a merging galaxy) and the other originates in a more “normal,” gaseous component, ionized by recent starbursts. The results of this test are clear: In Figure 5 *both* systems exhibit the high excitation conditions which are the signature of ionization by a strong UV continuum or by shock heating. Although there is more scatter in the points from regions  $> 7 \text{ kpc } h^{-1}$  from the nucleus, all fill a similar region

of the BPT diagrams, and all lie to the left (the AGN region) of the dividing line between AGN spectra and HII regions. Thus our first conclusion from this data is that there is no detectable starburst activity in the EELG.

### 3.3.2. Ionization/Excitation from a Central Source?

The diagrams in Figure 5 show no significant change in the line ratios as a function of distance. This is in general agreement with the conclusions of Danziger et al. 1984 and Robinson et al. 1987 that there is no appreciable change in the ionization parameter,  $U$ , of the EELG with radial distance from the central nuclear source. The conclusion they drew from this fact was that the gas density must decrease with radial distance. (Since  $U = \frac{Q}{4\pi c R^2 n_H}$ , where  $Q$  is the nuclear ionizing photon luminosity,  $R$  the radial distance from the nucleus, and  $n_H$ , the hydrogen number density, then if  $U$  is constant  $n_H$  must decrease.) However, a closer look at the BPT diagrams in Figure 5 and the [SII] plots in Figure 6a for points  $< 7 \text{ kpc } h^{-1}$  shows that the situation is more complex than this. The trend toward *increasing* density toward the east (seen in Figure 6a) does not fit into this picture. An increased density should lead to a *decreasing* ionization parameter (decreasing [OIII]/H $\beta$ ) in this direction, but the opposite is seen in Figure 5c and d. On the other hand, the clouds on the *western* side of the nucleus do seem to fit the central source picture. They tend to have lower ionization (lower [OIII]/H $\beta$ ) than those on the eastern side, and the increase in the [SII] ratios indicates that the clouds to the west also have decreasing density, balancing out the increase in  $R$ .

To help clarify this, the parameter which is most closely correlated with ionization ([OIII]/H $\beta$ , cf. Veilleux and Osterbrock 1987), is plotted as a function of radial distance in Figure 6b. Comparison of Figures 6a and b in the range  $-7 \leq R \leq 7$  shows that the trends predicted by a simple nuclear source photoionization model do not fit the observed density trends. These trends are significant within the measured errors and also consistent with the H $\alpha$  image of the gas (Figures 1b and 4b), which is fainter in the region to the west of the nucleus, showing that the gas there has a lower emission measure than the gas on the eastern side. We must conclude that either the gas on the western side of the EELG has  $n_H \sim R^{-2}$  with the number of ionizing photons falling off as  $R^{-2}$  while the eastern side is somehow receiving more ionizing photons at greater distances from the nucleus, or the

eastern EELG clouds have an additional source of ionization/excitation which supplements the nuclear source.

However, one interesting insight into the physical state of the EELG at  $R \geq 7 \text{ kpc } h^{-1}$  can be obtained from the simple central source model. Figure 6 shows that the lo-z system has lower densities and a higher  $U$  (higher [OIII]:H $\beta$ ) than the hi-z system. Thus, *if* the EELG is ionized by a central source, the relationship between  $U$  and  $n_H$  (given above) suggests that the two sets of clouds may well be at the same physical radius as well as the same projected radius from the nucleus.

While the above discussion is consistent with conclusions of Robinson et al. 1987, Storchi-Bergmann et al. 1996, and Wilson et al. 1997, where it was noted that different measured line ratios in PKS0349-27 were inconsistent with a global picture of ionization/excitation in the EELG based on photoionization by the (hidden) nuclear continuum, our findings are much more detailed and direct. The radial distributions of density and ionization reported here, coupled with the different characteristics of the two velocity systems seen in PA 83,<sup>o</sup> strongly suggest that whatever the final interpretation of this object, it must take the velocity systems into account.

In summary, these discrepancies in applying a central source model to the observed conditions in this galaxy's EELG when combined with the observation by Zirbel and Baum 1998 that its nucleus has little or no observed UV flux, implies that the source of at least some of the ionization/excitation observed in the extended gas has a non-nuclear origin.

### 3.3.3. Relationship Between the Different Velocity Systems?

In an attempt to identify common factors amongst gas clouds with  $R \geq 7 \text{ kpc } h^{-1}$  we have sorted them into the different velocity sets defined in section 3.2 (hi-lo-vel and hi-lo-z) and plotted the BPT diagrams shown in Figures 7 and 4. The plots with the most overlap (Figure 8) seem to be the ones in which the line ratios for the lo-z (A1 and B1) clouds are plotted together (Figure 8c and d). Almost all of these have values of [OIII]/H $\beta \geq 10$ . The hi-z clouds (A2 and B2, Figure 8a and b) also show good overlap and a slightly lower [OIII]/H $\beta$  value ( $\sim 8$ ) but with more scatter. What this means physically is that the gas in the lo-z clouds has a slightly higher ionization/excitation

state than that in the hi-z clouds. This is consistent with the [SII] line ratio plots in Figure 6a which indicate that the lo-z clouds have consistently lower densities, while the hi-z clouds show more scatter (see section 3.3.2 above).

If these similarities in ionization and density imply physical association, then the velocities in Figure 4a can be reconciled in the following way: Rotating the curves by  $180^\circ$  and shifting them in the radial direction (X-axis) by  $\sim 2.9$  kpc shows that the hook in the velocity curve at A1 and the flat region at B1 appear to be mirror images of the upper branch in the velocities at B2 and the flat part of the velocity plot at A2. However, this transformation does not fit the velocity points traced by the [SII] measurements, which we noted in Section 2.2.1 appeared to have three velocity components near the nucleus. These [SII] velocities seem to trace a system with a slightly negative velocity slope near the nucleus. Both of these features, asymmetrically shifted velocity curves which are mirror images, and small, inner systems which show counter rotation, are found in merging systems and tend to support the “merger” scenario for the origins of the gas (cf. MacKenty et al. 1994 and references therein).

### 3.4. Radio Jets and the EELG?

Although the symmetric velocity structure described in section 3.3.3 above may be consistent with a tidal-interaction/merger, the magnitude of the velocity separations between the two cloud systems is also consistent with the pattern of disruption caused by the passage of a radio jet<sup>3</sup>. The time scale for a disturbance in the gas to propagate from the location of the radio axis (at PA  $56^\circ$ ) to the observed position in the ionized gas at PA  $83^\circ$  when the gas is moving at a relative velocity of  $\sim 350$  km s<sup>-1</sup> is  $\sim 10^7$  years. This is comparable to the age of this type of FR II source ( $6\text{-}30 \times 10^6$  an, Carilli et al. 1991) and since the observed radial velocity differences between regions B1 and B2 and A1 and A2 exceed  $\sim 400$  km s<sup>-1</sup> at points, we cannot completely rule out collisional ionization of the EELG by the material ejected from the nucleus in a radio jet. However, there is some evidence that this type of jet-cloud collision generates ionization/excitation conditions which differ from both

those for AGN-like gas and HII regions (Simkin et al 1999b). In the few clear examples of an immediate jet-cloud collision (NGC 7385, Simkin et al. 1984, and Pictor A, Simkin et al. 1999a), the signature of such jet-ionized gas appears to be relatively low excitation (with a value of  $[\text{OIII}]/\text{H}\beta \leq 4$ ) along with AGN-like values of  $[\text{SII}]/\text{H}\alpha$  and  $[\text{OI}]/\text{H}\alpha$  but relatively lower values of  $[\text{NII}]/\text{H}\alpha$  (similar to those found for HII regions). The observed line ratios in Table 2 lie outside these ranges. This does not completely rule out the possibility that a past disturbance by a radio jet has ionized the gas in PKS0349-27, but the recombination times for gas at the densities indicated by the [SII] line ratios in Figure 6a will be shorter than the propagation time scale noted above and thus an additional source for the present ionization is still necessary.

## 4. Summary and Conclusions

Although the material reported here provides a much more detailed picture of the ionized gas in PKS0349-27 than previous observations, it raises several new questions.

On the positive side, these measurements point up the importance of the greater accuracy possible when diagnostic line ratios are analyzed in terms of the BPT scheme proposed by Veilleux and Osterbrock 1987. However, in spite of the observational advantages of this system, the discussions in sections 3.3.2 and 3.3 make it clear that it is difficult to compare the line ratio diagrams discussed here with either models or data reported in the more common systems which rely on  $[\text{OI}]:[\text{OIII}]$  or  $[\text{OII}]:[\text{OIII}]$  criteria for ionization/excitation determinations. Hopefully, there will be soon more detailed theoretical models which include published line ratios calculated for the Veilleux and Osterbrock 1987 system.

The present measurements lead to the following conclusions:

1. The ionization of the EELG in PKS0349-27 does not come from starburst activity.
2. The bifurcated velocity systems in PA  $83^\circ$  of this system appear to have similar emission line ratios (and thus similar ionization parameters) when grouped into hi-z and lo-z systems.
3. There may be yet a third velocity system near the nucleus of this system which is in counter rotation.

<sup>3</sup>We note that the “jet” seen at  $\sim \text{PA } 56^\circ$  in the original identification images by Searle and Bolton 1965 is most likely the inner part of the extended ionized gas seen in Figure 1b.



4. The gas clouds at projected distances closer than  $7 \text{ kpc } h^{-1}$  to the nucleus of PKS0349-27 have line ratios which are inconsistent with a simple central source ionization model and (particularly on the eastern side) require either an additional ionization source or a completely different mechanism which is unrelated to the nuclear source.
5. The most likely conclusion from these facts is that the gas has been disturbed by a merger or tidal interaction with a nearby galaxy, but the possibility of disruption by a radio jet cannot be completely ruled out.

On the other hand, there are several immediate questions raised by these data. Among the most obvious are:

1. What is the detailed velocity field of the EELG in PKS0349-27? Is the weaker, high velocity system only seen in PA  $83^\circ$  or does it extend into all areas around the nucleus?
2. What is the source of the “additional” ionization/excitation on the E side of the host? How can we distinguish between shock heating due to the merger of two galaxies and that caused by the passage of a radio jet?
3. What is the detailed radio structure (at arc second resolution) of PKS0349-27? Are the ionized gas filaments seen to the east of the nucleus interacting with the radio plasma? If so, what are the implications for the ionization/excitation of the EELG?

These questions underscore the need for new high resolution studies, with improved equipment (both radio and optical) of not only this object but also other nearby, FR II, radio galaxies for comparison.

This research has made use of the NASA/IPAC Extragalactic Database (NED) which is operated by the Jet Propulsion Laboratory, California Institute of Technology, under contract with the National Aeronautics and Space Administration. The CTIO observations were done with some support from NSF AST-89-14567 and publication costs from a grant (to SMS) from NASA, administered by the American Astronomical Society. The graphics in this paper were

generated with the software package *WIP*<sup>4</sup>, using the *PGPLOT*<sup>5</sup> graphics library.

## REFERENCES

- Allen, M., G., Dopita, M., A., Tsvetanov, Z., I., and Southerland, R., S., 1998, *ApJ*, 493, 571
- Arnaboldi, M.; Oosterloo, T.; Combes, F.; Freeman, K. C.; Koribalski, B., 1997, *AJ*, 113, 585
- Baldwin, J.A., Phillips, M.M., and Terlevich, R., 1981, *PASP*, 93, 5
- Baum, S. A., Heckman, T. M., Bridle, A., Van Breugel, W., Miley, G. K., 1988, *ApJS*, 68, 643
- Baum, S. A., and Heckman, T., 1989, *ApJ*, 336, 681
- Baum, S. A., and Heckman, T., 1989, *ApJ*, 336, 702
- Baum, S. A., Heckman, T. M., and Van Breugel, W., 1992, *ApJ*, 389, 208
- Best, P. N.; Longair, M. S.; Rottgering, H. J. A., 1996, *MNRAS*, 280, L9
- Binette, L., Wilson, A. S., Storchi-Bergmann, T., 1996, *A&AS*, 312, 365
- Bolton, J. G., Clarke, M. E., And Ekers, R. D., 1965, *Aust. J. Ph.*, 18, 627
- Byrd, G., G. and Klarić, M., 1990, *AJ*, 99, 1461
- Carilli, C. L.; Van Gorkom, J. H.; Stocke, John T., 1989, *Natur.* 338, 134
- Carilli, C. L., Perley, R. A., Dreher, J. W., and Leahy, J. P. 1991, *ApJ*, 383, 554
- Carilli, C. L.; Van Gorkom, J. H.; Stocke, John T. Van Gorkom, J. H.; Schweizer, Francois 1994, *AJ*, 107, 67
- Christiansen, W. N., Frater, R. F., And Watkinson, et al., 1977, *MNRAS*, 181, 183
- Danziger, I. J., Fosbury, R. A., Goss, W. M., Bland J. and Boksenberg, A., 1984, *MNRAS*, 208, 589

<sup>4</sup>*WIP* is copyright by the Berkeley-Illinois-Maryland Association (BIMA) Project (Morgan 1995)

<sup>5</sup>software copyrighted by California Institute of Technology

- Ekers, R. D., Wall, J. V., Shaver, W. M., Goss, W. M., Fosbury, R. A., Danziger, I. J., Moorwood, A. F. M., Malin, D. F., Monk, A. S., and Ekers, J. A., 1989, *MNRAS*, 236, 737
- Ferguson, J., W., Korista K., T., Baldwin J., A., and Ferland G., J. 1997, *ApJ*, 287, 122
- Hansen, L., Jorgensen, H. E., Norgaard-Nielsen, H. U., 1987, *A&AS*, 71, 465
- Hibbard, J.E., Guhathakurta, P., Van Gorkom, J.H., and Schweizer, F., 1996, *AJ*, 107, 67
- Hibbard, J.E. and Van Gorkom, J.H., 1996, *AJ*, 111, 655
- Koekemoer, A. M., Bicknell, G. V., 1998, *ApJ*, 497, 662
- MacKenty, J. W. 1986, *ApJ*, 308, 571
- MacKenty, J.W., Simkin, S.M., Griffith, R.E., Ulvestad, J.S., and Wilson, A.S. 1994, *ApJ*, 435, 71
- Mccarthy, Patrick J.; Spinrad, Hyron, Van Breugel, Wil, 1995, *ApJS*, 99, 27
- Mccarthy, Patrick J.; Baum, Stefi A.; Spinrad, Hyron, 1996, *ApJS*, 106, 281
- Morgan, J. A. 1995, in "Astronomical Data Analysis Software and Systems IV", *PASP Conf Series* 77, editors R. A. Shaw, H. E. Payne, and J. J. E. Hayes, p. 129
- Osterbrock D., 1989, in "Astrophysics of Gaseous Nebulae and Active Galactic Nuclei", (University Science Books, Mill Valley, CA), p. 134
- Perley, R.A., Röser, H.-J., and Meisenheimer, K. 1997, *A&A*, 328, 12
- Robinson, A., Binette, L., Fosbury, R. A., E., and Tadhunter, C. N., 1987, *MNRAS*, 227, 97
- Searle, L., and Bolton, J. G., 1968, *ApJ*, 154, 101
- Simkin, S. M., 1976, *ApJ*, 204, 251
- Simkin, S. M., Bicknell, G. V., and Bosma, A., 1984, *ApJ*, 277, 513
- Simkin, S. M. and Callcut, J., 1996, *IAU Symposium Number 175*, editors R. Ekers, C. Fanti, L. Padrielli, (Kluwer Academic Pub.), p.183
- Simkin, S. M. and Sadler, E. M., 1989, *IAU Symposium 134*, editors D. Osterbrock and J. Miller, (Kluwer, Dordrecht, The Netherlands), p. 484
- Simkin, S. M., Sadler, E. M., Sault, R., Tingay, S. J., and Callcut, J., 1999, *ApJ*(submitted, MS 39342)
- Simkin, S. M., Grimberg, B.I. and Sadler, E. M., 1999, *ApJ*, (in preparation)
- Storchi-Bergmann, T., Wilson, A., S., Mulchaey, J., S., and Binette, L., 1996, *A&A*, 312, 357
- Sulentic, J. W.; Marziani, P.; Zwitter, T.; Calvani, M., 1995, *ApJ*, 438, L1
- Tadhunter, C. N., Fosbury, R. A. E., and Quinn, P. J., 1989, *MNRAS*, 240, 225
- Tadhunter, C. N., Morganti, R., Robinson, A., Dickson, R., Villar-martin, M., Fosbury, R. A. E., 1998, *MNRAS*, 298, 1035
- Toomre, A., 1977, in *The Evolution of Galaxies and Stellar Populations*, edited by B. M. Tinsley and R. B. Larson (Yale University Observatory, New Haven), p.401
- van Breugel, Wh., Filippenko, A., V., Heckman, T., and Miley, G., 1985, *ApJ*, 293, 83
- Viegas, S.M. de Gouveia Dal Pino, E.M., 1992, *ApJ*, 384, 467
- Veilleux, S., and Osterbrock, D., 1987, *A&AS*, 63, 295
- Weaver, K. A.; Wilson, A. S.; Baldwin, J. A., 1991, *ApJ*, 366, 50
- Wilson, A. S., Binette, L., and Storchi-Bergmann, T., 1997, *ApJ*, 482, L131
- Zirbel, Esther L., and Baum, Stefi A., 1998 *ApJS*, 114, 177

TABLE 1  
CTIO - OPTICAL IMAGES AND SPECTRA

TELESCOPE	DATE	EXP TIME	AIRMASS	$\lambda_e$ (range)	$\Delta\lambda$	SEEING
CTIO-1.5m	22/23 Jan 1988	4000 s	1.02	7007Å	78-line	1.34''
CTIO-1.5m	22/23 Jan 1988	4000 s	1.12	6560Å	110-cont	1.24''
CTIO-1.5m	23/24 Jan 1988	4000 s	1.03	7007Å	78-line	1.39''
CTIO-1.5m	23/24 Jan 1988	4000 s	1.42	6560Å	110-cont	1.78''
CTIO-4m-PA 146°	15/16 Jan 1988	2000 s	1.30	6653-7338 Å	1.20 Å/px	1.43''
CTIO-4m-PA 83.1°	15/16 Jan 1988	2000 s	1.56	6653-7338 Å	1.20 Å/px	1.52''
CTIO-4m-PA 83.1°	16/17 Jan 1988	2000 s	1.19	4895-5745 Å	1.49 Å/px	1.67''

TABLE 2  
EMISSION LINE RATIOS IN PA 83.1°

R (kpc''h <sup>-1</sup> )	log( $\frac{[N II]}{H\alpha}$ )	log( $\frac{[S II]}{H\alpha}$ )	log( $\frac{[O III]}{H\beta}$ )	log( $\frac{[N II]}{H\alpha}$ )	log( $\frac{[S II]}{H\alpha}$ )	log( $\frac{[O III]}{H\beta}$ )
	A1 and B2			A2 and B1		
-14.72	0 <sup>+0.53</sup> <sub>-0.53</sub>	-0.02 <sup>+0.2</sup> <sub>-0.21</sub>	0.45 <sup>+0.08</sup> <sub>-0.08</sub>	-0.46 <sup>+0.15</sup> <sub>-0.19</sub>	-0.53 <sup>+0.17</sup> <sub>-0.22</sub>	0.84 <sup>+0.06</sup> <sub>-0.06</sub>
-14.02	...	...	...	-0.32 <sup>+0.05</sup> <sub>-0.05</sub>	-0.44 <sup>+0.06</sup> <sub>-0.06</sub>	1.39 <sup>+0.21</sup> <sub>-0.15</sub>
-13.32	-0.17 <sup>+0.08</sup> <sub>-0.08</sub>	-0.12 <sup>+0.07</sup> <sub>-0.08</sub>	1.05 <sup>+0.07</sup> <sub>-0.06</sub>	...	...	...
-12.61	-0.21 <sup>+0.1</sup> <sub>-0.1</sub>	-0.31 <sup>+0.11</sup> <sub>-0.12</sub>	1.26 <sup>+0.21</sup> <sub>-0.15</sub>	-0.34 <sup>+0.17</sup> <sub>-0.2</sub>	-0.51 <sup>+0.22</sup> <sub>-0.3</sub>	1.45 <sup>+0.61</sup> <sub>-0.25</sub>
-11.91	-0.14 <sup>+0.08</sup> <sub>-0.08</sub>	-0.17 <sup>+0.08</sup> <sub>-0.09</sub>	0.91 <sup>+0.08</sup> <sub>-0.07</sub>	-0.1 <sup>+0.1</sup> <sub>-0.11</sub>	-0.51 <sup>+0.18</sup> <sub>-0.23</sub>	0.79 <sup>+0.1</sup> <sub>-0.08</sub>
-11.21	-0.18 <sup>+0.06</sup> <sub>-0.06</sub>	-0.28 <sup>+0.07</sup> <sub>-0.07</sub>	0.97 <sup>+0.06</sup> <sub>-0.05</sub>	-0.38 <sup>+0.18</sup> <sub>-0.22</sub>	-0.2 <sup>+0.14</sup> <sub>-0.15</sub>	1.01 <sup>+0.11</sup> <sub>-0.09</sub>
-10.51	-0.28 <sup>+0.06</sup> <sub>-0.06</sub>	-0.31 <sup>+0.06</sup> <sub>-0.06</sub>	1.12 <sup>+0.08</sup> <sub>-0.07</sub>	-0.03 <sup>+0.08</sup> <sub>-0.1</sub>	-0.07 <sup>+0.1</sup> <sub>-0.11</sub>	0.75 <sup>+0.1</sup> <sub>-0.09</sub>
-9.81	-0.21 <sup>+0.04</sup> <sub>-0.05</sub>	-0.25 <sup>+0.05</sup> <sub>-0.05</sub>	1.12 <sup>+0.07</sup> <sub>-0.06</sub>	-0.24 <sup>+0.12</sup> <sub>-0.13</sub>	-0.25 <sup>+0.12</sup> <sub>-0.13</sub>	0.79 <sup>+0.14</sup> <sub>-0.12</sub>
-9.11	...	...	...	0.03 <sup>+0.22</sup> <sub>-0.21</sub>	0.04 <sup>+0.21</sup> <sub>-0.21</sub>	0.76 <sup>+0.17</sup> <sub>-0.13</sub>
-8.41	0.06 <sup>+0.16</sup> <sub>-0.15</sub>	-0.23 <sup>+0.21</sup> <sub>-0.24</sub>	-0.02 <sup>+0.15</sup> <sub>-0.15</sub> 1	-0.35 <sup>+0.08</sup> <sub>-0.09</sub>	-0.26 <sup>+0.08</sup> <sub>-0.08</sub>	1.57 <sup>+0.61</sup> <sub>-0.25</sub>
-7.71	-0.15 <sup>+0.1</sup> <sub>-0.11</sub>	-0.24 <sup>+0.12</sup> <sub>-0.12</sub>	1.18 <sup>+0.21</sup> <sub>-0.15</sub>	...	...	...
-7.01	-0.26 <sup>+0.15</sup> <sub>-0.17</sub>	-0.35 <sup>+0.17</sup> <sub>-0.2</sub>	1.02 <sup>+0.15</sup> <sub>-0.12</sub>	...	...	...
-6.31	-0.32 <sup>+0.12</sup> <sub>-0.13</sub>	0.04 <sup>+0.08</sup> <sub>-0.08</sub>	1.06 <sup>+0.17</sup> <sub>-0.13</sub>	...	...	...
-4.91	-0.61 <sup>+0.14</sup> <sub>-0.18</sub>	-0.4 <sup>+0.1</sup> <sub>-0.12</sub>	0.91 <sup>+0.07</sup> <sub>-0.06</sub>	...	...	...
-4.2	-0.39 <sup>+0.14</sup> <sub>-0.17</sub>	-0.12 <sup>+0.1</sup> <sub>-0.1</sub>	1.16 <sup>+0.13</sup> <sub>-0.1</sub>	...	...	...
-3.5	-0.45 <sup>+0.14</sup> <sub>-0.16</sub>	-0.09 <sup>+0.09</sup> <sub>-0.09</sub>	0.97 <sup>+0.1</sup> <sub>-0.08</sub>	...	...	...
-2.8	-0.09 <sup>+0.08</sup> <sub>-0.08</sub>	-0.03 <sup>+0.07</sup> <sub>-0.07</sub>	1.19 <sup>+0.11</sup> <sub>-0.09</sub>	...	...	...
-2.1	-0.27 <sup>+0.08</sup> <sub>-0.09</sub>	-0.21 <sup>+0.08</sup> <sub>-0.08</sub>	0.85 <sup>+0.04</sup> <sub>-0.03</sub>	...	...	...
-1.4	-0.19 <sup>+0.05</sup> <sub>-0.05</sub>	-0.16 <sup>+0.05</sup> <sub>-0.05</sub>	1.07 <sup>+0.11</sup> <sub>-0.09</sub>	...	...	...
-0.7	-0.05 <sup>+0.03</sup> <sub>-0.03</sub>	-0.09 <sup>+0.03</sup> <sub>-0.03</sub>	0.85 <sup>+0.04</sup> <sub>-0.04</sub>	...	...	...
0	-0.05 <sup>+0.05</sup> <sub>-0.05</sub>	-0.06 <sup>+0.04</sup> <sub>-0.04</sub>	0.87 <sup>+0.07</sup> <sub>-0.03</sub>	...	...	...
0.7	-0.03 <sup>+0.03</sup> <sub>-0.03</sub>	0.01 <sup>+0.03</sup> <sub>-0.03</sub>	0.91 <sup>+0.06</sup> <sub>-0.06</sub>	...	...	...
1.4	-0.02 <sup>+0.03</sup> <sub>-0.03</sub>	0.12 <sup>+0.03</sup> <sub>-0.03</sub>	0.74 <sup>+0.06</sup> <sub>-0.05</sub>	...	...	...
2.1	0.02 <sup>+0.05</sup> <sub>-0.05</sub>	0.21 <sup>+0.04</sup> <sub>-0.04</sub>	0.51 <sup>+0.07</sup> <sub>-0.07</sub>	...	...	...
6.31	0.08 <sup>+0.21</sup> <sub>-0.2</sub>	0.25 <sup>+0.18</sup> <sub>-0.16</sub>	0.45 <sup>+0.24</sup> <sub>-0.19</sub>	...	...	...
3.5	-0.27 <sup>+0.18</sup> <sub>-0.21</sub>	0.31 <sup>+0.1</sup> <sub>-0.1</sub>	1.03 <sup>+0.09</sup> <sub>-0.07</sub>	...	...	...
4.2	-0.22 <sup>+0.13</sup> <sub>-0.15</sub>	0.18 <sup>+0.09</sup> <sub>-0.09</sub>	0.55 <sup>+0.08</sup> <sub>-0.08</sub>	...	...	...
7.01	-0.07 <sup>+0.29</sup> <sub>-0.31</sub>	0.06 <sup>+0.26</sup> <sub>-0.25</sub>	0.34 <sup>+0.13</sup> <sub>-0.11</sub>	...	...	...
7.71	-0.39 <sup>+0.21</sup> <sub>-0.27</sub>	-0.12 <sup>+0.15</sup> <sub>-0.16</sub>	0.73 <sup>+0.14</sup> <sub>-0.12</sub>	...	...	...
8.41	-0.57 <sup>+0.11</sup> <sub>-0.13</sub>	-0.7 <sup>+0.13</sup> <sub>-0.17</sub>	0.64 <sup>+0.24</sup> <sub>-0.18</sub>	...	...	...
9.11	-0.1 <sup>+0.15</sup> <sub>-0.15</sub>	-0.52 <sup>+0.25</sup> <sub>-0.36</sub>	1.68 <sup>+0.69</sup> <sub>-0.69</sub>	-0.55 <sup>+0.1</sup> <sub>-0.11</sub>	-0.59 <sup>+0.11</sup> <sub>-0.13</sub>	1.26 <sup>+0.14</sup> <sub>-0.11</sub>
9.81	-0.05 <sup>+0.11</sup> <sub>-0.11</sub>	-0.3 <sup>+0.15</sup> <sub>-0.16</sub>	0.98 <sup>+0.24</sup> <sub>-0.16</sub>	-0.68 <sup>+0.07</sup> <sub>-0.08</sub>	-0.62 <sup>+0.07</sup> <sub>-0.07</sub>	1.27 <sup>+0.2</sup> <sub>-0.14</sub>
10.51	-0.3 <sup>+0.16</sup> <sub>-0.18</sub>	-0.21 <sup>+0.14</sup> <sub>-0.16</sub>	0.79 <sup>+0.16</sup> <sub>-0.13</sub>	-0.43 <sup>+0.06</sup> <sub>-0.07</sub>	-0.5 <sup>+0.07</sup> <sub>-0.08</sub>	1.02 <sup>+0.04</sup> <sub>-0.04</sub>
11.21	-0.2 <sup>+0.09</sup> <sub>-0.09</sub>	-0.41 <sup>+0.11</sup> <sub>-0.13</sub>	0.71 <sup>+0.09</sup> <sub>-0.08</sub>	-0.49 <sup>+0.05</sup> <sub>-0.05</sub>	-0.5 <sup>+0.05</sup> <sub>-0.05</sub>	1.08 <sup>+0.06</sup> <sub>-0.05</sub>
11.91	-0.21 <sup>+0.06</sup> <sub>-0.07</sub>	-0.76 <sup>+0.15</sup> <sub>-0.2</sub>	0.69 <sup>+0.14</sup> <sub>-0.11</sub>	-0.35 <sup>+0.05</sup> <sub>-0.05</sub>	-0.31 <sup>+0.05</sup> <sub>-0.05</sub>	1.24 <sup>+0.08</sup> <sub>-0.07</sub>
12.61	...	...	...	-0.29 <sup>+0.09</sup> <sub>-0.1</sub>	0 <sup>+1.1</sup> <sub>-0</sub>	0.99 <sup>+0.11</sup> <sub>-0.09</sub>

**Grimberg, Sadler, and Simkin; EELG-PKS0349-27**

Figure 1. (a) Optical continuum image of PKS349-027 with slit positions (white) and direction of the radio axis (black) shown. (b)  $H\alpha$  image produced by subtracting a model of the continuum in (a). Nucleus is marked with a cross.

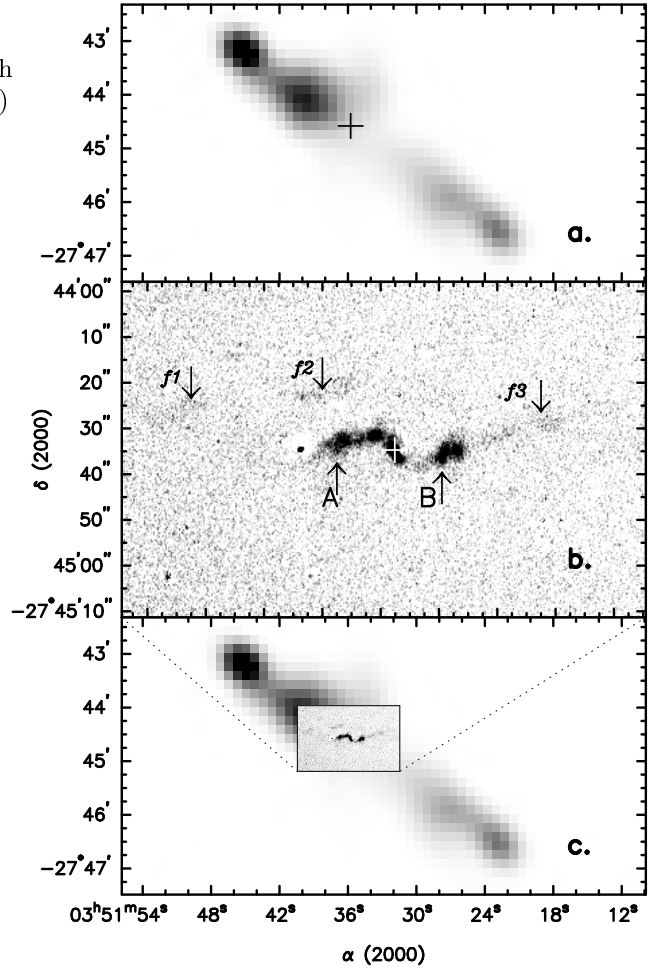
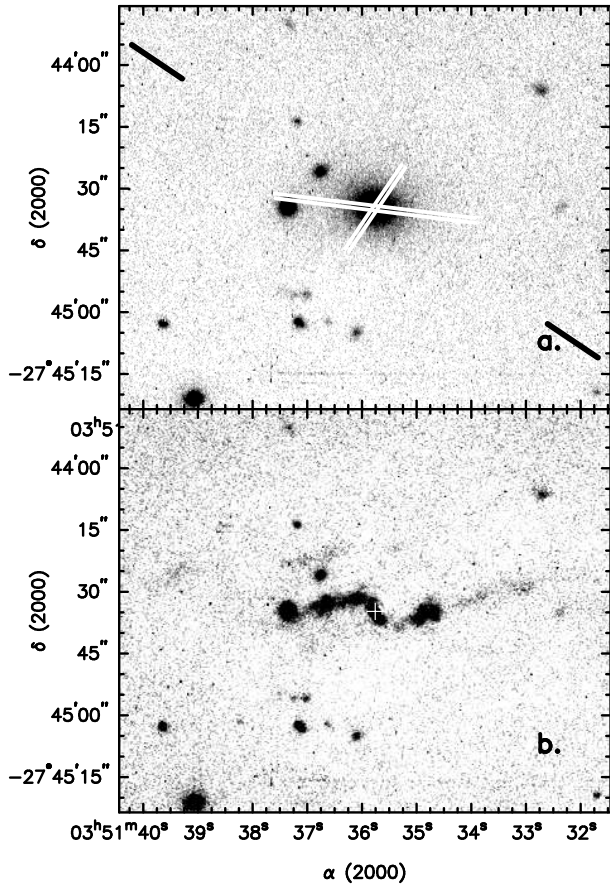


Figure 2 (a) 20 cm VLA continuum image of PKS349-027; position of the optical nucleus is marked with a cross. (b) the  $H\alpha$  image produced by subtracting continuum image in Figure 1a from the narrow-band  $7007\text{\AA}$  image. Note that the only objects in the field which are not continuum sources are the “z” shaped structure centered on the nucleus (with an extended, faint filament to the W, marked  $f3$ ) and the two disconnected patches  $f1$  and  $f2$  respectively). The knots marked A and B correspond to prominent spectral features in figs 3 and 4. (c) Shows the relationship of the  $H\alpha$  image in (b) to the radio structure.

Figure 1. (a) Emission lines of  $H\alpha$  and  $[NII]$  in PA  $83^\circ$ . (b) Emission lines of  $[OIII]$ , 5007/4958 in PA  $83^\circ$ . Y-axes are scaled to the same velocity units and zeroed to the rest frame of the galaxy. Positions A1, A2, B1, and B2 correspond to knots marked A and B in fig 2b.

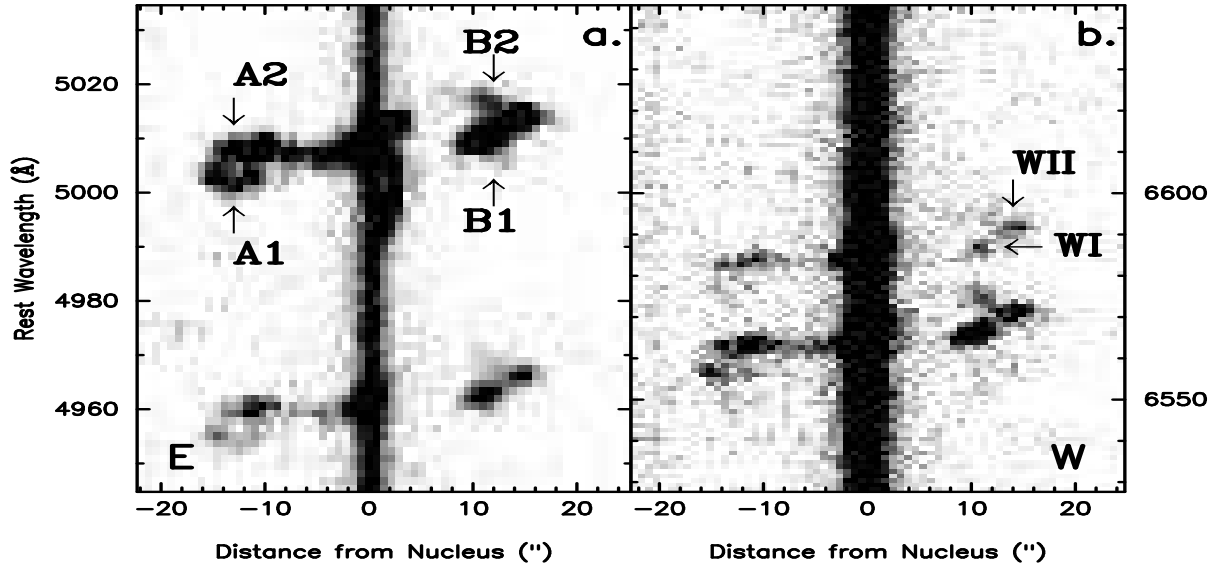


Figure 4 Optical velocities for PKS0349-027 in PA  $83^\circ$  (a) and PA  $146^\circ$  (b). Clouds A1, A2, B1, and B correspond to knots marked A and B in fig 2b and corresponding spectral features marked in fig 3a.

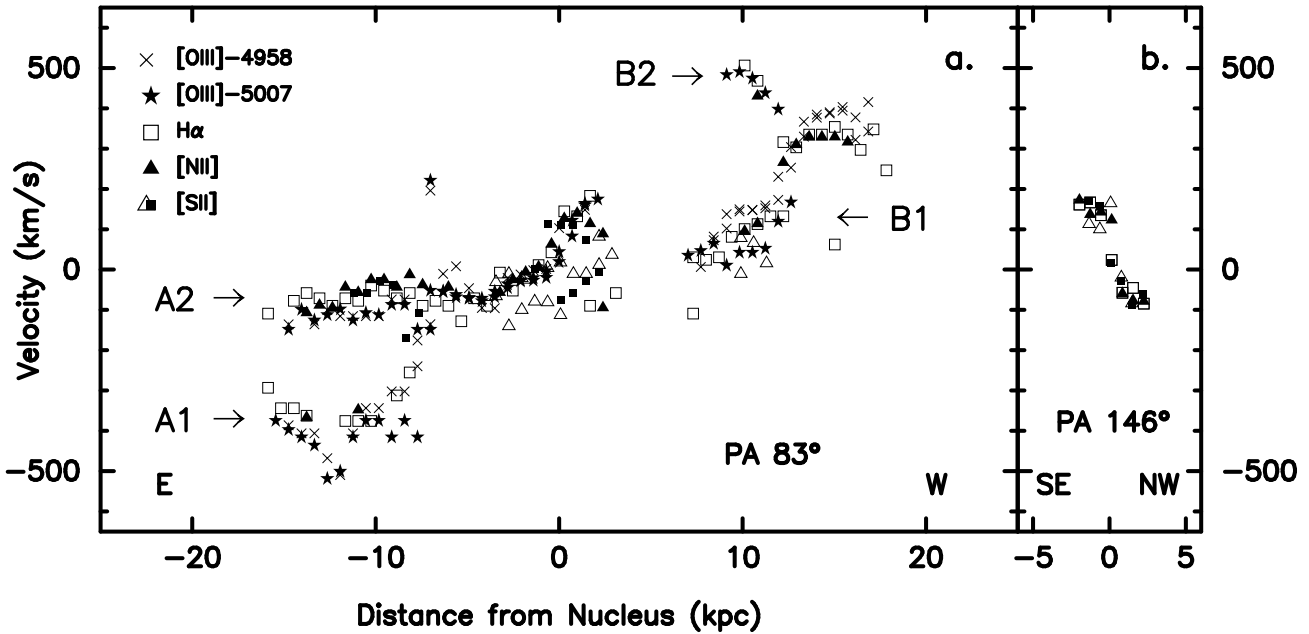


Figure 5. BPT Diagrams for the gas in PKS340-027 along PA83.<sup>o</sup> (a and b) show the [SII] and [NII] plots for the outer part of the “z” shaped emission regions and (c and d) show similar plots for regions closer to the nucleus.

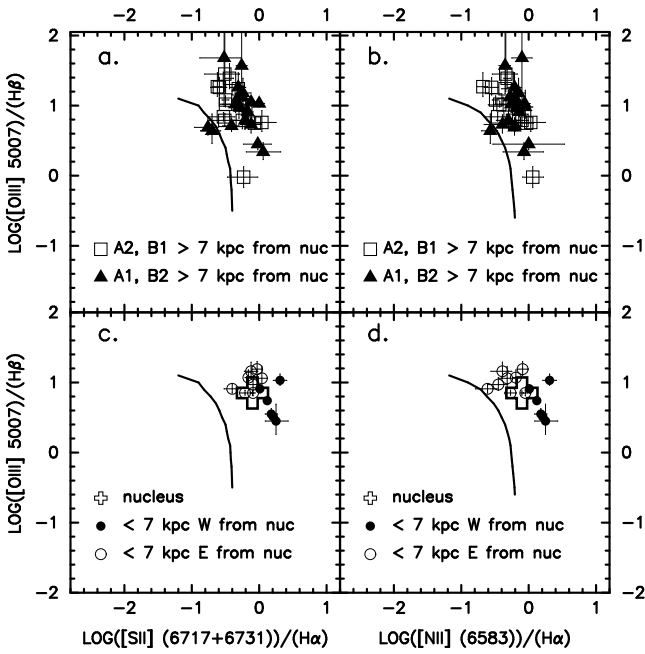


Figure 6. (a) [SII] line ratios for the EELG in regions A and B plotted against projected radial distance from the nucleus. (b) [OIII]:Hβ line ratios plotted in the same way. Higher values indicate a larger ionization parameter  $U$ .

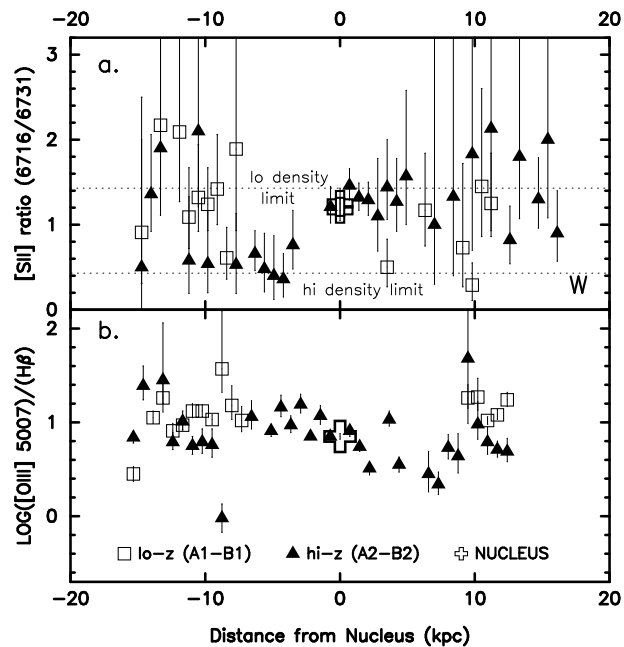


Figure 7. (a) BPT Diagrams for the extended gas clouds in regions A and B (a and b) show the relationship (A2) clouds between 7 and 15 kpc to the east of the nucleus and (c and d) show similar plots for the to the west of the nucleus.

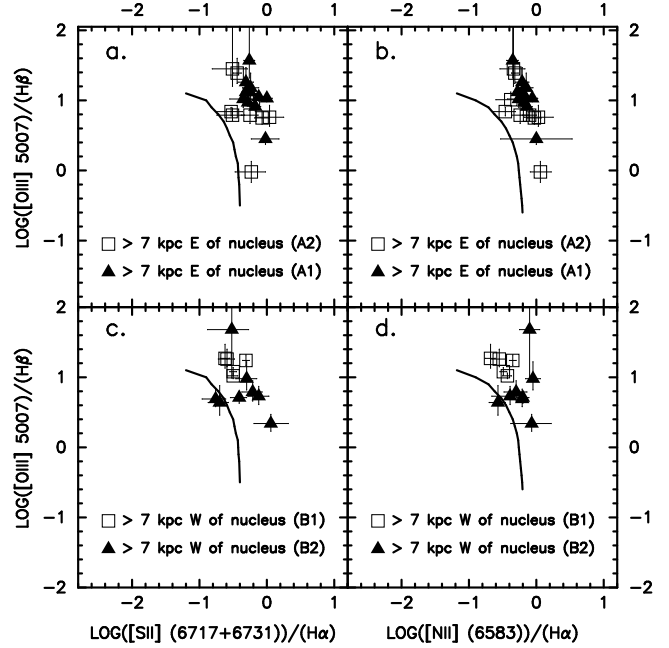


Figure 8 BPT Diagrams for the extended gas clouds in regions A and B (a and b) show the relationship between the clouds with high systemic redshift (A2 and B2), and (c and d) show the relationship between the clouds with lower systemic redshift (A1 and B1).

